

Multiarmed Aromatic Ammonium Salts Boost the Efficiency and Stability of Inverted Organic Solar Cells

Yufei Xin,[#] Hang Liu,[#] Xiyue Dong, Zheng Xiao, Rui Wang, Yuping Gao, Yu Zou, Bin Kan, Xiangjian Wan, Yongsheng Liu,^{*} and Yongsheng Chen^{*}



Cite This: *J. Am. Chem. Soc.* 2024, 146, 3363–3372



Read Online

ACCESS |



Metrics & More

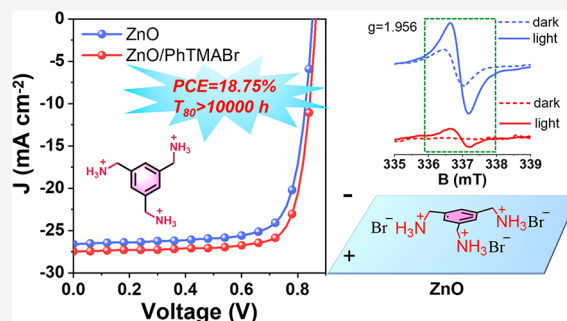


Article Recommendations



Supporting Information

ABSTRACT: Inverted organic solar cells (OSCs) have attracted much attention because of their outstanding stability, with zinc oxide (ZnO) being commonly used as the electron transport layer (ETL). However, both surface defects and the photocatalytic effect of ZnO could lead to serious photodegradation of acceptor materials. This, in turn, hampers the improvement of the efficiency and stability in OSCs. Herein, we developed a multiarmed aromatic ammonium salt, namely, benzene-1,3,5-triyltrimethanaminium bromide (PhTMABr), for modifying ZnO. This compound possesses mild weak acidity aimed at removing the residual amines present within ZnO film. In addition, the PhTMABr could also passivate surface defects of ZnO through multiple hydrogen-bonding interactions between its terminal amino groups and the oxygen anion of ZnO, leading to a better interface contact, which effectively enhances charge transport. As a result, an efficiency of 18.75% was achieved based on the modified ETL compared to the bare ZnO (PCE = 17.34%). The devices utilizing the modified ZnO retained 87% and 90% of their initial PCE after thermal stress aging at 65 °C for 1500 h and continuous 1-sun illumination with maximum power point (MPP) tracking for 1780 h, respectively. Importantly, the extrapolated T_{80} lifetime with MPP tracking exceeds 10 000 h. The new class of materials employed in this work to modify the ZnO ETL should pave the way for enhancing the efficiency and stability of OSCs, potentially advancing their commercialization process.



1. INTRODUCTION

Organic solar cells (OSCs) are considered as a promising photovoltaic technology due to their unique advantages, such as light weight, flexibility, and environmental friendliness.^{1–6} Benefiting from the rapid developments of polymer donors and non-fullerene acceptors (NFAs), a certified power conversion efficiency (PCE) of 19.4% has been achieved for conventional OSCs with p–i–n structure utilizing PEDOT:PSS as the hole transport layer (HTL).^{7–15} However, the poor stability of conventional OSCs arising from the corrosivity and hygroscopicity of PEDOT:PSS hinders their further commercialization process. Therefore, it is necessary to obtain a delicate balance between device efficiency and operational stability.

Recently, inverted OSCs with n–i–p structure have attracted significant attention due to their distinguished stability when compared with conventional OSCs.^{16–19} Zinc oxide (ZnO) is widely used as the electron transport layer (ETL) in such structures.^{19,20} Typically, the ZnO film exhibits both high electron mobility and exceptional transmittance from visible to near-infrared light.^{21–23} This film possesses an energy level of 4.30 eV for the conduction band minimum (E_{CBM}) and 7.2 eV for the valence band maximum (E_{VBM}), providing a suitable energy level arrangement between the ETL and the active layer.^{24,25} Note that the distortion of

tetrahedral angles in ZnO results in a difference in electronegativity between unsaturated Zn and O ions.^{26,27} This disparity, when exposed to illumination, gives rise to radicals, leading to the degradation of NFAs—a phenomenon acknowledged as the photocatalytic effect.

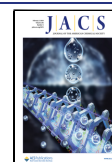
Generally, the ZnO films can be in situ synthesized by the sol–gel method using quantitative amine with appropriate base dissociation constants (pK_b) to control its cluster size and composition.^{27–29} However, the amine residues could accelerate the degradation of NFAs at the ZnO/BHJ interface due to photogenerated radicals in ZnO. This amine-induced coordination or redox reaction will enhance photocatalysis activity, thereby significantly degrades device performance and stability.^{27,30} In addition, various vacancy defects existing on the surface of ZnO films could generate a mass of recombination centers, leading to insufficient charge extraction and transportation.³¹ In the past few years, small molecular

Received: November 10, 2023

Revised: December 27, 2023

Accepted: December 27, 2023

Published: January 24, 2024



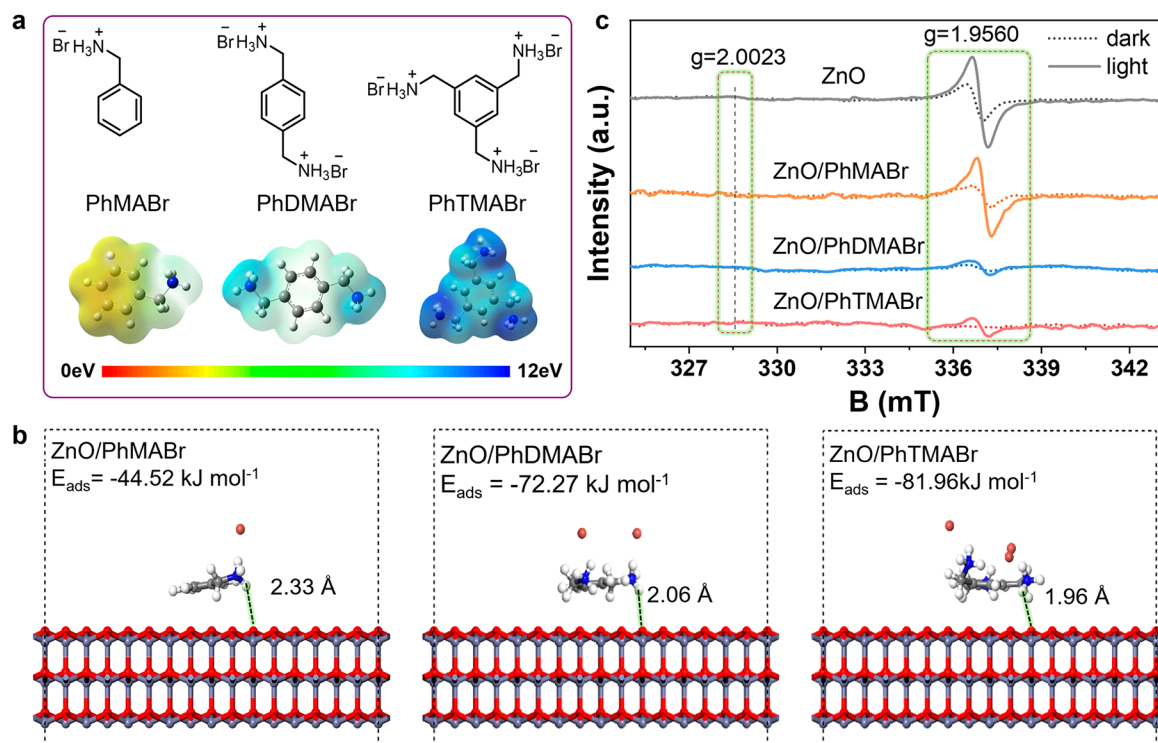


Figure 1. (a) Chemical structures and ESP maps of PhMABr, PhDMABr, and PhTMABr. (b) Optimized configurations of PhMABr, PhDMABr, and PhTMABr after being adsorbed on the ZnO surface. (c) EPR spectra of ZnO powders with and without organic ammonium modification. Note that these powders were obtained by scraping off the corresponding films from the substrates.

acids have been used for ZnO modification to solve the above problems. Chen and co-workers utilized an organic conjugated small-molecule acid named 2-(3-(dimethylamino)propyl)-1,3-dioxo-2,3-dihydro-1*H*-benzo[*de*]isoquinoline-6,7-dicarboxylic acid (NMA) to modify the ZnO layer, achieving a significantly improved overall device performance (PCE = 18.2%) and photostability (T_{80} lifetime = 7572 h).³² Hou et al. employed boric acid (BA) to suppress the photocatalysis effect of the ZnO film, achieving an efficiency of 18.4% and a lifetime over 9000 h.²⁶ However, the efficiency of inverted organic solar cells still lags far behind that of state-of-the-art conventional OSCs. Therefore, it is imperative to develop efficient strategies for passivating surface defects and suppressing the photocatalysis in ZnO to further improve the efficiency and stability of the devices. Small molecular acid salts may have the potential to modify the ZnO layer by passivating the photogenerated radicals in ZnO film, thereby enhancing device performance and stability. However, small molecular acid salts have rarely been reported to modify the ZnO in OSCs.

Herein, we proposed a class of aromatic ammonium salts with weak acidity to modify the ZnO for passivating the defects and protecting the active layer from photocatalytic oxidation. This strategy has been successfully demonstrated by developing a series of aromatic amine hydrobromides, namely, phenylmethanaminium bromide (PhMABr), 1,4-phenylenedimethanaminium bromide (PhDMABr), and benzene-1,3,5-triyltrimethanaminium bromide (PhTMABr), respectively. The calculated results for the adsorption energy between aromatic ammonium salts and ZnO indicate that ZnO/PhTMABr exhibits the highest stability. This could be attributed to the robust hydrogen-bonding interaction (N–H...O) between the proton in the terminal amino group and the oxygen anions in ZnO as confirmed by the shift of the

–NH₃ group in ¹H NMR spectra. Such interactions have the potential to immobilize oxygen anions and reduce the photocatalytic activity. Moreover, PhTMABr plays a key role as an interfacial dipole, which can reduce the charge transport resistance and enhance charge transport and extraction in comparison with the pristine ZnO. As a result, the PM6:L8-BO:BTP-eC9-based device using PhTMABr-treated ZnO ETL achieves a champion PCE of 18.75% compared with that of the bare ZnO device (PCE = 17.34%). Benefiting from the enhanced stability of BHJ films, the device based on ZnO/PhTMABr can maintain 87% and 90% of its initial PCE under 65 °C thermal aging for 1500 h and maximum power point (MPP) tracking for 1780 h. Besides, the extrapolated T_{80} lifetime of the device is 10619 h, which is the longest T_{80} lifetime among inverted OSCs with a PCE larger than 18.5%, illustrating the distinguished reliability of the novel modification method.

2. RESULTS AND DISCUSSION

The synthetic routes and detailed procedures of PhMABr, PhDMABr, and PhTMABr are shown in the [Supporting Information](#). According to the molecular electrostatic surface potential (ESP) distribution calculated by density functional theory (DFT) calculations (B3LYP/6-31G*) (Figure 1a), the positive electricity of the terminal ammonium ions increased gradually from PhMABr to PhTMABr, which could account for the incremental adsorption energy with ZnO (Figure 1b). The adsorption energy of ZnO/PhTMABr is $-81.96 \text{ kJ mol}^{-1}$, which is twice that of ZnO/PhMABr. This indicates that the ZnO/PhTMABr configuration is more stable. Moreover, we found that the interaction distance decreased gradually when PhMABr, PhDMABr, and PhTMABr were adsorbed on the

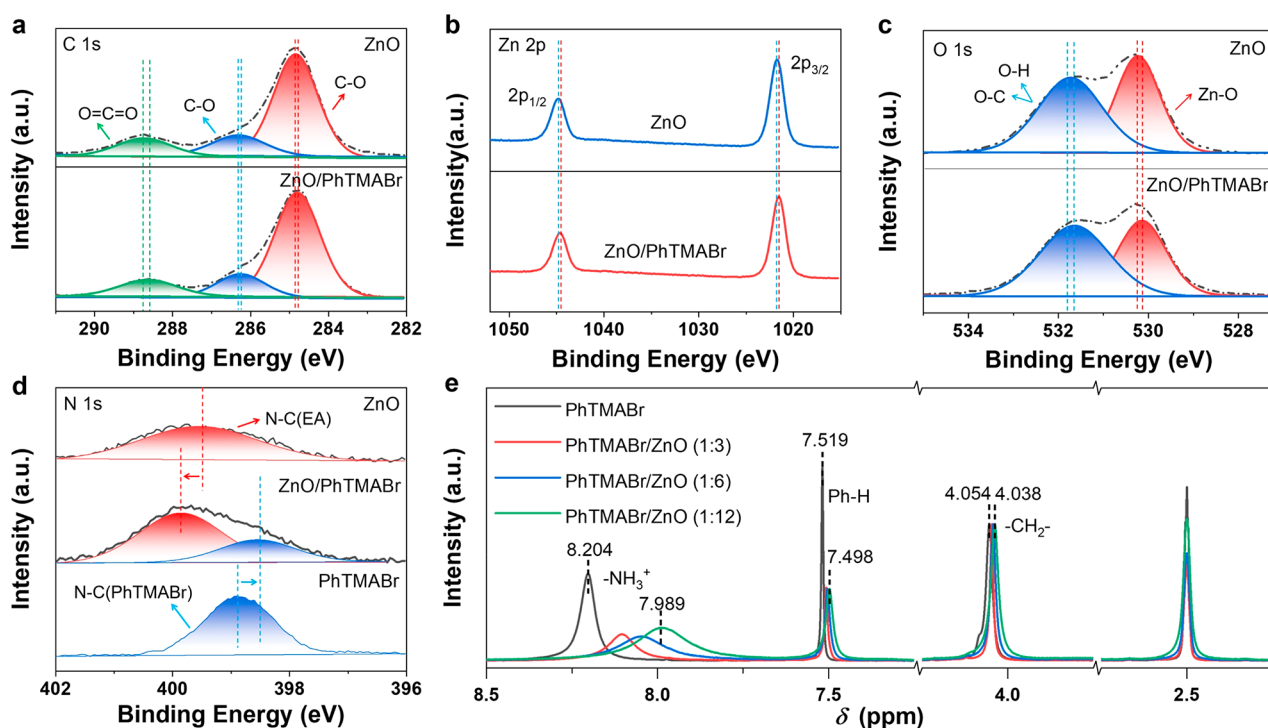


Figure 2. (a–d) XPS spectra of pristine ZnO and ZnO/PhTMABr, respectively. (a) C 1s, (b) Zn 2p, (c) O 1s, and (d) N 1s. (e) ^1H NMR of pristine PhTMABr/ZnO in $\text{DMSO-}d_6$ with different molar ratios.

ZnO surface, reducing from 2.33 Å to 1.96 Å. These distances are in the hydrogen bond range.

The photocatalysis of ZnO originates from surface radicals and vacancy defects, leading to unfavorable charge transportation and degradation of the active layer. To assess the photocatalytic activity of ZnO with and without our modified layer, we conducted electron-paramagnetic resonance (EPR) spectroscopy measurements on samples under dark and light illuminations. As shown in Figure 1c, two distinct signals at $g = 2.0023$ and $g = 1.9560$ were observed. The former is attributed to surface Zn vacancies, and the latter is generally associated with shallow donors caused by surface oxygen vacancies and interstitial Zn atoms.^{33,34} Under dark conditions, the intensities of both signals decreased, indicating reduced concentrations of vacancy defects and radicals. Upon 10 min illumination, a significant increase in the signals at $g = 1.9560$ was observed compared to those at $g = 2.0023$, suggesting that photoinduced charge transfer primarily originates from surface oxygen vacancies and interstitial Zn atoms. The amplification in the signal at $g = 1.9560$ is particularly pronounced in unprocessed ZnO, indicating more serious photocatalysis. From ZnO/PhMABr to ZnO/PhTMABr, the amplification of the peak at $g = 1.9560$ decreased gradually, especially for ZnO/PhDMABr and ZnO/PhTMABr. This trend suggests that the photocatalytic activity is highly restrained, which is beneficial for the charge transport of ZnO and the stability of the active layer.

The electric conductivity (σ) of ZnO/PhTMABr and ZnO/PhDMABr ETLs was calculated to be 3.64×10^{-3} and $3.22 \times 10^{-3} \text{ S m}^{-1}$, respectively, which is higher than that of bare ZnO ($2.3 \times 10^{-3} \text{ S m}^{-1}$), as illustrated in Figure S1. However, the σ of ZnO/PhMABr ETL is $2.4 \times 10^{-3} \text{ S m}^{-1}$, which is close to the control ZnO ETL. The improved conductivity could be attributed to the reduction of the vacancy defects, the suppression of the redox reaction, and the pre-movement of impurity ions in the surface after the modification of ZnO with

PhTMABr or PhDMABr.³⁵ To preliminarily estimate the photovoltaic performance of our designed materials for ZnO modification, the PM6:L8-BO (chemical structure in Figure S2)¹¹ binary bulk heterojunction (BHJ) was selected to fabricate devices with an inverted structure of ITO/ETL/PM6:L8-BO/MoO₃/Ag. The current density–voltage (J – V) curves of the devices based on the different ETLs are shown in Figure S3, and the detailed parameters are summarized in Table S1. The device based on pristine ZnO ETL exhibited an inferior PCE of 17.10%, with an open-circuit voltage (V_{OC}) of 0.874 V, a short-circuit current density (J_{SC}) of 25.21 mA cm^{-2} , and a fill factor (FF) of 77.57%. After modification of the ZnO film with a thin PhTMABr layer, the V_{OC} , J_{SC} , and FF of the device were synergistically enhanced to 0.893 V, 26.08 mA cm^{-2} , and 79.03%, respectively, yielding an outstanding PCE of 18.43%. Besides, an efficiency improvement was also observed in the device using a PhDMABr-processed ZnO layer (PCE = 18.00%). However, the device based on ZnO/PhMABr only showed a slight improvement with a PCE of 17.20%. The morphology of BHJ films on these ETLs, showing little difference, was not the critical factor affecting the device efficiency (Figure S4). The relatively poor photovoltaic performance of the devices based on the PhMABr-processed ZnO film could be ascribed to the weak interaction between ZnO and PhMABr, resulting in ineffective defect passivation. Combining the above electric conductivity and EPR analysis, we can conclude that PhTMABr can serve as the most promising material for ZnO passivation to reduce vacancy defects and suppress the photocatalysis in ZnO among these hydrobromides. Our subsequent research will focus on this aspect.

The residual amine in ZnO originating from the sol–gel method will lead to coordination or redox reaction with Zn, resulting in unfavorable amine doping of ZnO with enhanced photocatalytic activity, which could induce the degradation of

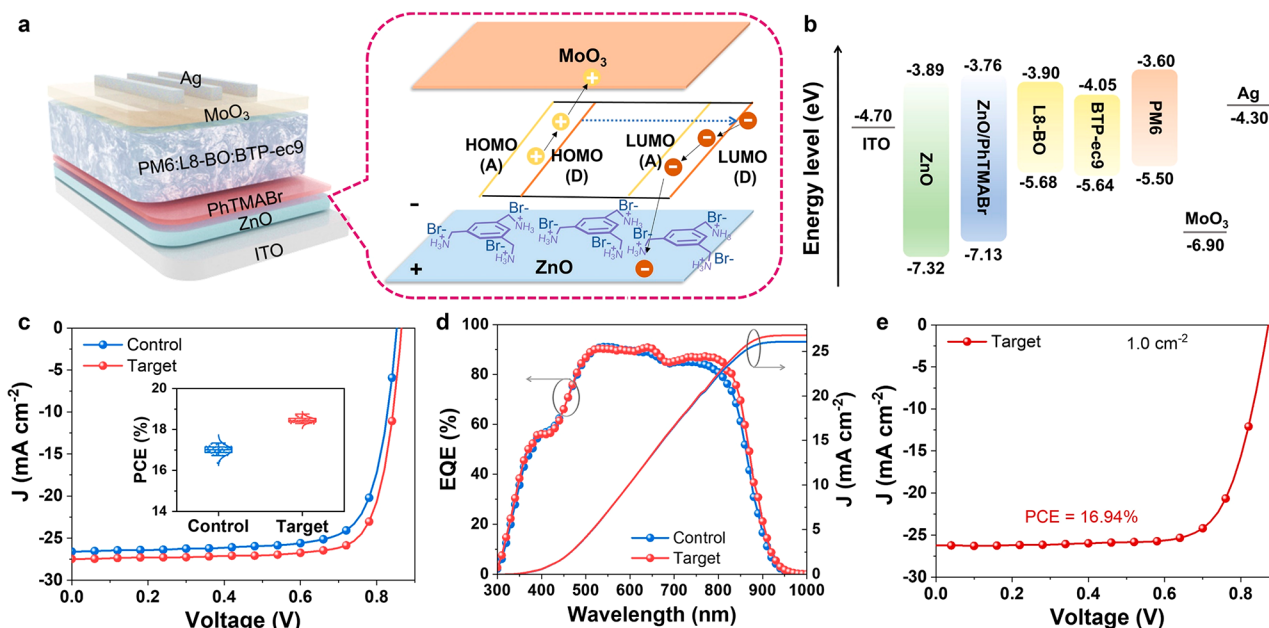


Figure 3. (a) Schematic illustration of the device structure and the interaction between ZnO and PhTMABr as a dipole. Inset is the PCE distribution (30 individual devices were collected) of the control and target devices. (b) Energy level diagram of materials involved in this work. (c) J - V characteristics curves of the PM6:L8-BO:BTP-ec9 device based on two ETLs. (d) EQE spectra and integrated photocurrent density of the corresponding devices. (e) J - V curve of a large-area device (area: 1.0 cm²) based on OSC with PhTMABr-treated ZnO ETL.

NFAs.^{27,36} To gain a deeper understanding of the chemical species on the ZnO ETL surface, we carried out X-ray photoelectron spectroscopy (XPS) measurements. As shown in Figure 2a, three peaks in the C 1s region, corresponding to -C-C, C-O, and carboxyl bonds at 284.8, 286.3, and 288.7 eV, respectively, were identified. These peaks were attributed to the following sources: (1) residual ethanolamine (EA) and the intermediate hydrolysate ammonium acetate in ZnO by sol-gel fabrication; (2) the PhTMABr layer spin-coated on ZnO; and (3) adventitious "carbon and carbonate" present in the ambient environment.^{37,38} After modification, a deviant range of 0.2 eV moving toward lower binding energy was observed in the above three peaks, indicating the interaction between two layers. In the Zn region (Figure 2b), the Zn 2p_{1/2} and Zn 2p_{3/2} peaks appeared at 1044.9 and 1021.8 eV in pristine ZnO. Similarly, these peaks moved to 1044.7 and 1021.6 eV, respectively, due to the reduced oxygen vacancy or Zn vacancies.³⁶ The reduced oxygen vacancy can suppress the photocatalysis effect in ZnO as discussed in the EPR analysis. The observed trend aligns closely with the O 1s (Figure 2c) XPS analysis, a consistent shift in energy of the O-Zn bond peak from 530.3 to 530.1 eV after PhTMABr modification. In addition, the decreased intensity of the peak for the O-Zn bond could be attributed to the reduced amine-doped ZnO. The moved shoulder peak from 531.8 eV to 531.5 eV can be ascribed to ·OH and O-C, which originates from the changed amount of superoxide anion or ·OH radical on the surface of ZnO/PhTMABr.²⁷ The N 1s XPS analysis of ZnO/PhTMABr shown in Figure 2d exhibits a peak shift from 399.5 eV to 399.9 eV corresponding to the N-C bond of EA.^{26,27} Besides, the reducing peak area can be considered to be empirical evidence that the residual amine and ammonium carboxylate were partially removed through rinsing with a PhTMABr solution. Simultaneously, a new peak at 398.5 eV ascribed to the N-C bond of PhTMABr was observed. This peak was introduced by the PhTMABr layer coated on ZnO, consistent

with the N 1s XPS spectra of PhTMABr powders. In the ZnO film treated with PhTMABr, the N-C bond of EA from the ZnO fabrication process shifted toward higher binding energy. Conversely, the corresponding N-C bond in PhTMABr shifted from 399.1 eV to 398.5 eV, confirming the strong interaction between ZnO and PhTMABr.

To further elucidate the interaction mechanism between ZnO and PhTMABr, ¹H NMR characterization was carried out in the deuterated dimethyl sulfoxide (DMSO-*d*₆) suspension of PhTMABr with different molar ratios of ZnO powders scraped off from the substrate (Figure 2e and Figures S5-S7). For the pristine PhTMABr solution, the proton peaks of the terminal amino group (NH₃⁺), benzene ring (Ph-H), and methylene (-CH₂-) were located at 8.204, 7.519, and 4.054 ppm, respectively. After mixing with ZnO powders, the chemical shifts of these peaks moved toward a higher field, attributed to the shielding effect between ZnO and protons of PhTMABr. This effect could be caused by the oxygen anions in ZnO. In particular, the chemical shift of the protons in NH₃⁺ exhibited a significant shift from 8.204 ppm to 7.989 ppm with the incremental ZnO proportion, much more than those in Ph-H and -CH₂-. Besides, the shape of this NH₃⁺ peak became wider, but the area remained the same, demonstrating that the proton in NH₃⁺ was in hydrogen bond association (N-H...O) with the negative oxygen ions in ZnO, in agreement with the DFT calculation results discussed above. Note that a similar trend was observed for solutions based on ZnO/PhMABr and ZnO/PhDMABr in ¹H NMR characterization (Figures S8 and S9).

Ultraviolet photoelectron spectroscopy (UPS) was employed to determine the work function (W_F) of ZnO before and after modification. As depicted in Figure S10, the secondary-electron cutoffs (E_{cutoff}) of ZnO and ZnO/PhTMABr are located at 17.26 and 17.39 eV, respectively, with a 0.13 eV offset. Relative to the Fermi level (E_{Fermi}) of referenced Au (21.22 eV), the W_F values of ZnO and ZnO/

Table 1. Optimized Photovoltaic Parameters for Devices Based on ZnO or ZnO/PhTMABr

BHJ	ETLs	V_{OC} [V]	J_{SC} [mA cm^{-2}]	J_{SC}^{a} [mA cm^{-2}]	FF [%]	PCE _{max} /PCE _{avg} [%]
PM6:L8-BO:BTP-ec9	ZnO	0.853	26.60	26.10	76.47	17.34
		0.853 ± 0.007	26.20 ± 0.60		76.24 ± 0.85	17.00 ± 0.38
	ZnO/PhTMABr	0.865	27.46	26.82	78.95	18.75
		0.865 ± 0.006	27.20 ± 0.35		78.47 ± 0.71	18.49 ± 0.25

^aCalculated from EQE data.

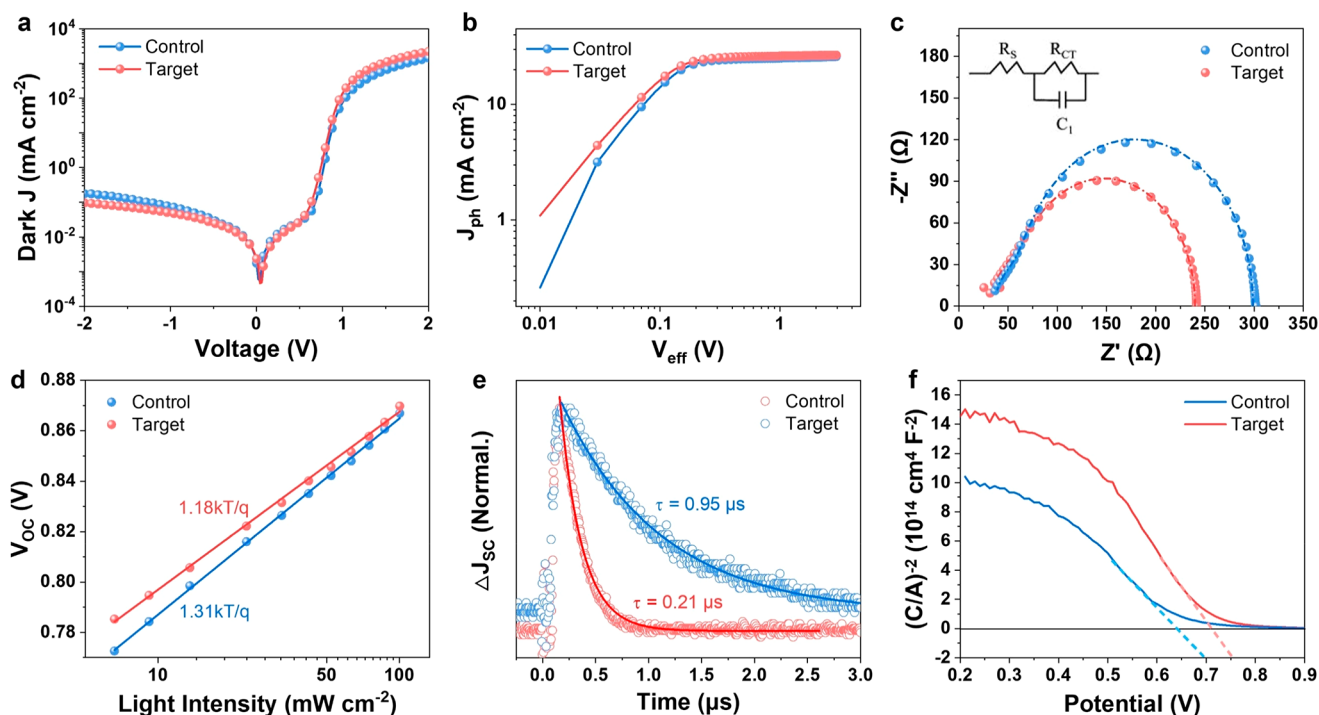


Figure 4. (a) J - V characteristic curves of the devices based on two ETLs in the dark state. (b) Photocurrent density versus effective voltage (J_{ph} - V_{eff}) characteristics for the corresponding devices. (c) Nyquist plots of control and target devices. Inset: The equivalent-circuit model employed for fitting of EIS data. (d) Semilogarithmic plots of V_{OC} versus light intensity. (e) Transient photocurrent measurements of devices analyzed by a single-exponential decline model. (f) Mott-Schottky plots of devices based on the studied ETLs. Note: Control and target represent the devices based on ZnO and ZnO/PhTMABr, respectively.

PhTMABr are 3.96 and 3.83 eV, respectively. The decreased W_F , resulting from the elimination of excess amine doping in ZnO, is advantageous for establishing an improved ohmic contact with an organic photoactive layer.³⁰ The reduced diiodomethane contact angle from 30.64° to 26.81° (Figure S11) and decreased root-mean-square (RMS) roughness of ZnO film (Figure S12) after modification indicate the surface processing of ZnO with PhTMABr could enhance the interface contact between the organic active layer with the substrate.

The BTP-ec9 (chemical structure in Figure S2) with narrower bandgap was chosen as the third component of PM6:L8-BO binary BHJ to study the device performance and device physics based on the ZnO/PhTMABr ETL. Figure 3a presents the device structure along with a schematic illustration of the ZnO/PhTMABr interface. This illustration highlights how PhTMABr can serve as a dipole to improve the built-in electric field and promote the exciton dissociation at the interface of donor/acceptor. The conduction band (CB) of ZnO/PhTMABr was calculated to be -3.76 eV based on the UPS results and optical bandgap (Figure S13). This value is slightly higher than that of pristine ZnO, which is beneficial for the transportation and collection of electrons. The energy level arrangement in Figure 3b indicates that the ZnO film treated

with PhTMABr exhibits an up-shifted CB due to the elimination of excess amine doping in ZnO. This is consistent with a smaller W_F , which is favorable to the electron transportation. Figure 3c shows the current density-voltage (J - V) curves of the optimized devices, with detailed photovoltaic parameters summarized in Table 1. The device based on the pristine ZnO ETL exhibits a V_{OC} of 0.853 V, a J_{SC} of 26.60 mA cm^{-2} , and an FF of 76.47%, yielding a PCE of 17.34%. After treating the ZnO film with PhTMABr, the optimized PCE (Figure S14a, Table S2) was boosted to 18.75% with a V_{OC} of 0.865 V, a J_{SC} of 27.46 mA cm^{-2} , and an FF of 78.95%, which is a record PCE for inverted OSCs based on a ZnO ETL to the best of our knowledge.^{26,32,39} Importantly, the devices based on ZnO/PhTMABr demonstrate excellent reproducibility, with an average PCE of 18.49%, significantly surpassing that of the control devices (PCE_{avg} = 17.00%) (Figure 3c). As illustrated in Figure 3d, the calculated J_{SC} from external quantum efficiency (EQE) data was 26.10 and 26.82 mA cm^{-2} for the devices based on ZnO without and with PhTMABr, respectively. This aligns well with the J - V data with an error within 3%. The higher EQE response in the NFA region demonstrated the enhanced charge collection of the device using PhTMABr-modified ZnO.

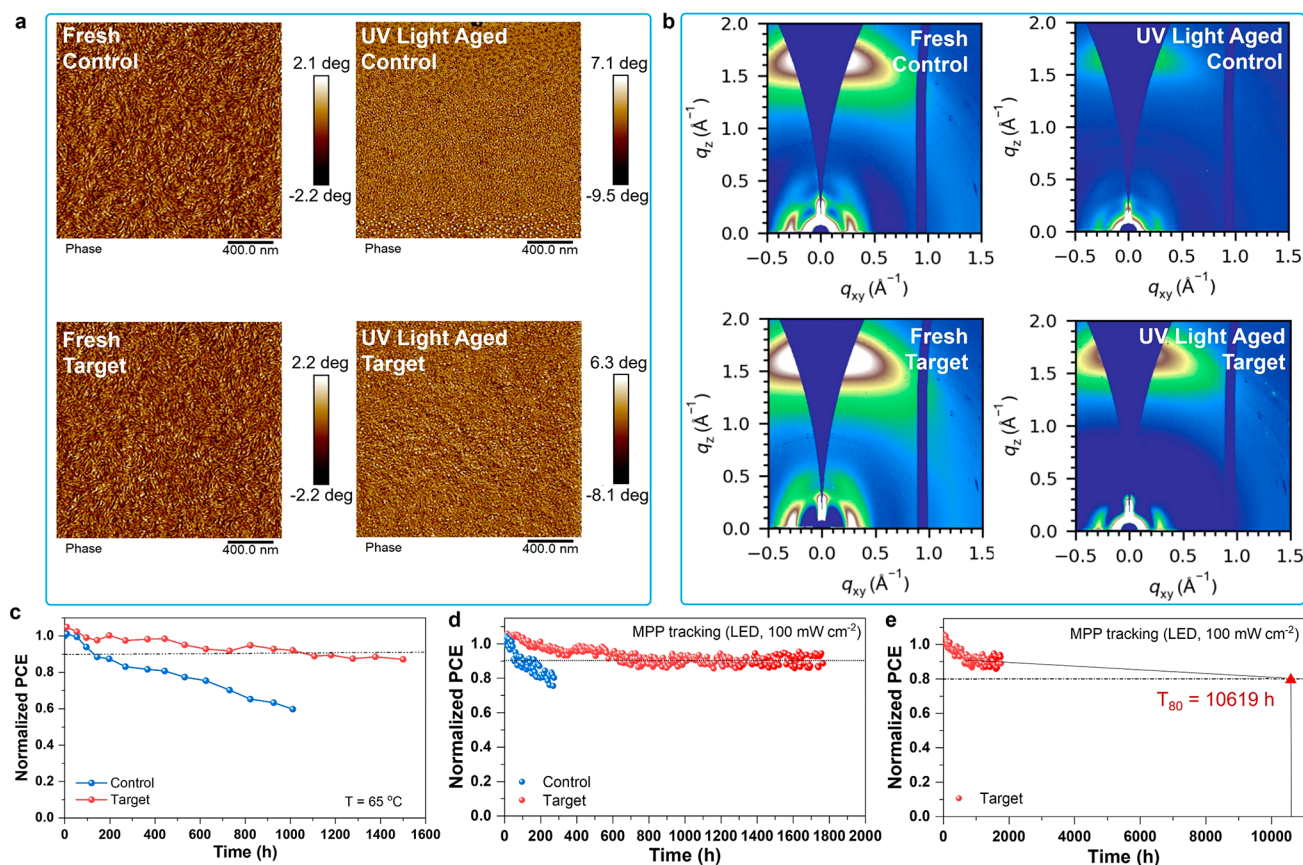


Figure 5. (a) AFM phase images of the control and target film before and after 72 h UV illumination. (b) GIWAXS patterns for PM6:L8-BO:BTP-ec9 films based on two ETLs before and after 72 h UV illumination. (c) Thermal aging test of unencapsulated devices based on ZnO and ZnO/PhTMABr under 65 °C in a N₂ glovebox. (d) Unencapsulated devices under MPP tracking with continuous illumination (100 mW cm⁻², white LED) in a N₂ atmosphere. (e) T₈₀ analysis of the device based on ITO/ZnO/PhTMABr/PM6:L8-BO:BTP-ec9/MoO₃/Ag. The black line is a linear fit for extraction of T₈₀ from 740 to 1800 h.

Given the high performance of the device based on ZnO/PhTMABr, the OSCs with active areas of 1.0 cm² were also fabricated. As shown in Figure 3e, the best-performing large-area device measured under standard AM 1.5 G conditions showed a V_{OC} of 0.872 V, a J_{SC} of 26.23 mA cm⁻², and an FF of 74.05%, respectively, yielding a high PCE of 16.94%. Note that we have evaluated organic salts based on PhTMA with different anions, including PhTMACl and PhTMAI, and have achieved comparable device performance (Figure S14b, Table S3). When using PFNBr to process a ZnO film, a PCE of 17.9% was obtained, which is lower than that of the PhTMABr-based device (Figure S14c, Table S3). Moreover, various BHJ systems have been employed to validate the universality of this ZnO/PhTMABr ETL, all of which demonstrated enhanced device performance (Figure S15, Table S4).

The significantly improved device performance could be attributed to enhanced charge transport and suppressed recombination, which can be characterized by device physics. The exciton dissociation and charge collection properties of the OSCs with the two ETLs were initially evaluated. Figure 4a illustrates the J - V characteristics of OSCs in the dark state. A reduced leakage current under a reverse bias voltage was observed in the ZnO/PhTMABr-based device, indicating the suppression of hole injection at the cathode interface.^{40,41} At a positive bias, the current density of the ZnO/PhTMABr-based device is higher than that of the control, which can be

attributed to a smaller series resistance. Figure 4b displays curves of the photocurrent density (J_{ph}) with respect to effective bias. In contrast to the device with an unmodified ZnO ETL, the dissociation probabilities $P(E,T)$ of the devices using PhTMABr-modified ZnO ETL were improved from 96.0% to 98.0% (for the short-circuit condition) and from 86.2% to 88.2% (for the maximal power output condition). This improvement suggests that less driving force is needed to extract the carriers from the device.⁴² In addition, we measured the Nyquist plot of the electrochemical impedance spectroscopy (EIS) spectra for OSCs based on different ETLs (Figure 4c). According to the equivalent-circuit model,⁴³ the series resistance (R_{series}) and charge-transport resistance (R_{CT}) are 34.2 and 267.6 Ω for the control devices and 32.8 and 207.3 Ω for the target devices, respectively. The reduction in both R_{series} and R_{CT} indicates fewer interfacial defects and better contact between the ETL and BHJ after modification. This improvement is beneficial for suppressing charge recombination.

To further verify the carrier recombination in the control and target device, light intensity (I)-dependent J - V characteristics were assessed.⁴⁴ After modification, the exponent α of the target device ($J_{SC} \propto I^\alpha$) increased from 0.986 to 0.991 (Figure S16), indicating weaker bimolecular recombination, leading to improved FF and J_{SC} . The light intensity-dependent V_{OC} data following the equation $V_{OC} \propto nkT/q \ln(I)$ show that the target device exhibits a reduced slope of 1.18kT/q compared to that of the control device (1.31kT/q) (Figure 4d). The slope closer

to kT/q suggests suppressed trap-assisted recombination loss in the target device. Moreover, transient photocurrent (TPC) and transient photovoltage (TPV) measurements were carried out to estimate the charge-carrier dynamic. The TPC curves in Figure 4e showed that the target device exhibited a shorter decay time of 0.21 μs in comparison with the control ($\tau = 0.95 \mu\text{s}$), where the shorter decay time represents the faster charge collection. As confirmed by the TPV results (Figure S17), the target device showed a much longer carrier lifetime of 400 μs in comparison with the control device ($\tau = 105 \mu\text{s}$). The longer carrier lifetimes suggest suppressed nonradiative recombination in the target device, resulting in an improved V_{OC} . To assess the nonradiative recombination photovoltage loss ($\Delta V_{\text{OC,nr}}$), the external electroluminescence yield (EQE_{EL}) was measured against the injection current by operating the OSC device as a light-emitting diode (LED). As shown in Figure S18, the target device exhibits a higher EQE_{EL} of 6.8×10^{-5} than that of the control device (4.2×10^{-5}). The nonradiative energy loss (ΔE_{nr}) of the photovoltaic device was calculated using the formula $\Delta E_{\text{nr}} = -kT \ln(\text{EQE}_{\text{EL}})$, where T is the absolute temperature and k is the Boltzmann constant.⁴⁵ The calculated ΔE_{nr} for the target device is 0.248 eV, which is lower than that of the control device (0.260 eV). This result is consistent with the improved V_{OC} of the target device.

To investigate the difference in the built-in voltage (V_{bi}) of devices induced by the PhTMABr-treated ZnO in comparison with the control ZnO, a Mott–Schottky analysis was performed. As illustrated in Figure 4f, the target device based on PhTMABr-treated ZnO exhibits a higher V_{bi} of 0.752 V in comparison with the control device ($V_{\text{bi}} = 0.696 \text{ V}$). The larger V_{bi} can be attributed to the smaller W_{F} of the ZnO/PhTMABr film, which could promote the drift current across the entire device, resulting in a slightly enlarged V_{OC} .⁴⁶

The long-term stability is one of the key factors restricting the practical application of OSCs. To explore the influence of modified ZnO on stability, we first access the morphology stability of the BHJ film under continuous UV illumination in ambient conditions. As shown in Figure 5a, the atomic force microscope (AFM) images of BHJ films on both ETLs show a favorable bicontinuous double-fibril network at first. Subsequently, the BHJ film on ZnO/PhTMABr maintains nearly constant roughness (Figure S19) and continues to exhibit a well-organized, fiberlike structure after 72 h, demonstrating excellent UV light aging stability. However, the morphology of the BHJ film on bare ZnO has changed from a fibril network to a complete spherical shape after 72 h of UV illumination. This change suggests a significant increase in phase separation, likely induced by the photocatalysis effect within the ZnO film, which leads to the dissociation of NFAs on the ZnO/BHJ interface.^{26,32} The increased UV light aging stability of the BHJ film on a ZnO substrate treated with PhTMABr indicates that PhTMABr may mitigate the photocatalysis effect of ZnO, possibly because the residual amine was removed through the modification of ZnO with PhTMABr, leading to a reduction in photogenerated radicals.

Moreover, the UV–vis absorption spectra of BHJ films and neat NFA films on both the bare and PhTMABr-processed ZnO substrate were measured to access intrinsic chemical changes with or without UV illumination. As shown in Figure S20a, the intensity of two absorption peaks in the control film representing PM6 and acceptors both substantially reduced to nearly 20% of the initial value after 72 h of UV illumination. At the same condition, the equivalent absorption peak of the

target film modified with PhTMABr can maintain 88% of its initial intensity, suggesting the improved stability of BHJ films. Similarly, in the neat NFAs films, as shown in Figure S20b, the absorption intensity at λ_{max} of the control and target film decreased 48.1% and 0.9%, respectively, compared with their initial intensity, indicating dissociation of NFAs under UV illumination, in agreement with the above AFM analysis. Grazing incidence wide-angle X-ray diffraction (GIWAXS) characterization (Figure 5b) was conducted to investigate the impact of ZnO/PhTMABr on the molecular packing in BHJ films. The stronger π – π stacking at 1.72 \AA^{-1} in the out-of-plane (OOP) direction and lamellar stacking at 0.28 \AA^{-1} in the in-plane (IP) direction were observed in the target film. This observation is beneficial for the charge transport in the device.⁴¹ Based on the OOP and IP line cut profiles (Figure S20), the crystalline coherence length (CCL) was calculated by the following equation:^{47,48}

$$\text{CCL} = 2\pi k / \text{fwhm} \quad (1)$$

where fwhm is the half-width of the diffraction peak and k equals 0.9.⁴⁹ Here, ΔCCL was employed to highlight the variation in CCL for the π – π stacking of fresh and aged BHJ films, as defined by the following equation:¹⁸

$$\Delta\text{CCL} = (\text{CCL}_{\text{aged}} - \text{CCL}_{\text{fresh}}) / \text{CCL}_{\text{fresh}} \times 100\% \quad (2)$$

The CCL of fresh and aged BHJ films on ZnO/PhTMABr is 24.06 and 23.76 \AA ($\Delta\text{CCL} = -1.25\%$), respectively. In contrast, the CCL of BHJ films on bare ZnO decreased from 18.66 \AA (fresh) to 16.63 \AA (aged) ($\Delta\text{CCL} = -10.88\%$). The larger CCL of π – π stacking in the BHJ film on the ZnO/PhTMABr substrate is beneficial to the carrier transportation,^{50–52} resulting in improved J_{SC} and FF. The smaller ΔCCL indicates that the molecular packing stability in the BHJ film has enhanced when using the PhTMABr-processed ZnO as substrate. Note that we also explored alternative aromatic ammonium salts, such as 2,5-thiophenedimethylammonium bromide (ThDMABr), for the modification of the ZnO film. Comparatively, the film stability of both the BHJ and NFA films, as well as the device performance, exhibited obvious improvement compared to films or devices based on pristine ZnO ETL (Figures S14c and S21, Table S3).

To investigate the influence of the PhTMABr layer on device stability, the sequential characterization included studying the variation in PCE under thermal aging and while operating at MPP. As shown in Figure 5c, the PM6:L8-BO:BTP-ec9 device based on ZnO/PhTMABr maintained 87.3% of its initial PCE after annealing at 65 $^{\circ}\text{C}$ for 1500 h. In contrast, the PCE of the ZnO-based device was significantly reduced to 59% after 1100 h. We further access the operational stability operated at an MPP under 100 mW cm^{-2} light illumination (white LED, $T = 55 \text{ }^{\circ}\text{C}$, light spectrum in Figure S22). As shown in Figure 5d, the PCE of the champion target device remained at 90.0% of its initial value after 1780 h, whereas the control device substantially decreased to 77.3% within 270 h, mainly resulting from sharply degraded J_{SC} and FF. The increased device stability is consistent with the optimized film morphology, increased chemical stability, and molecular packing of the BHJ film on the ZnO substrate treated with PhTMABr. The extrapolated T_{80} lifetime of the target device obtained by fitting the linearly decaying part is 10 619 h (Figure 5e). Note that this is the longest T_{80} lifetime among inverted OSCs with a PCE exceeding 18.5%, to our best knowledge.^{26,32,39}

3. CONCLUSION

In conclusion, we have successfully demonstrated a novel method to improve the efficiency and stability of inverted OSCs by modifying the ZnO layer with multiarmed aromatic ammonium salts. It is found that there are strong hydrogen-bonding interactions (N–H...O) between the proton in the terminal amino group with the oxygen anions in ZnO, resulting in reduced vacancy defects. The processing of ZnO with PhTMABr could not only reduce the interfacial impedance and inhibit trap-assisted recombination but also protect the BHJ layer from photocatalytic degradation when it directly contacts the ZnO layer. As a result, the optimized PM6:L8-BO:BTP-ec9 devices using PhTMABr-processed ZnO as the ETL achieved a champion PCE of 18.75%. Importantly, the BHJ films on a PhTMABr-modified ZnO ETL exhibit a superior UV aging stability. Benefiting from the improved stability of BHJ films, the devices based on ZnO/PhTMABr maintained 90% of their initial efficiency under MPP tracking (white light LED, 100 mW cm⁻²) for 1780 h, whereas the control device decreased to 77.3% of its initial value after 270 h. Besides, the extrapolated T₈₀ lifetime of the device by linear fitting is 10 619 h, illustrating the distinguished reliability of the novel modification method. This work offers a promising avenue to enhance the efficiency and stability of organic solar cells.

■ ASSOCIATED CONTENT

SI Supporting Information

The Supporting Information is available free of charge at <https://pubs.acs.org/doi/10.1021/jacs.3c12605>.

Materials synthesis, EPR, XPS, UPS, AFM, UV–vis, GIWAXS, EIS, TPC, J_{ph} – V_{eff} measurements, device characterization and stability measurements, theoretical calculations, ¹H NMR and ¹³C NMR data (PDF)

■ AUTHOR INFORMATION

Corresponding Authors

Yongsheng Liu – *The Centre of Nanoscale Science and Technology and Key Laboratory of Functional Polymer Materials, Institute of Polymer Chemistry, College of Chemistry and Renewable Energy Conversion and Storage Center (RECAST), Nankai University, Tianjin 300071, China; orcid.org/0000-0002-7135-723X; Email: liuys@nankai.edu.cn*

Yongsheng Chen – *The Centre of Nanoscale Science and Technology and Key Laboratory of Functional Polymer Materials, Institute of Polymer Chemistry, College of Chemistry and Renewable Energy Conversion and Storage Center (RECAST), Nankai University, Tianjin 300071, China; orcid.org/0000-0003-1448-8177; Email: yschen99@nankai.edu.cn*

Authors

Yufei Xin – *The Centre of Nanoscale Science and Technology and Key Laboratory of Functional Polymer Materials, Institute of Polymer Chemistry, College of Chemistry, Nankai University, Tianjin 300071, China*

Hang Liu – *The Centre of Nanoscale Science and Technology and Key Laboratory of Functional Polymer Materials, Institute of Polymer Chemistry, College of Chemistry, Nankai University, Tianjin 300071, China*

Xiyue Dong – *The Centre of Nanoscale Science and Technology and Key Laboratory of Functional Polymer*

Materials, Institute of Polymer Chemistry, College of Chemistry, Nankai University, Tianjin 300071, China

Zheng Xiao – *The Centre of Nanoscale Science and Technology and Key Laboratory of Functional Polymer Materials, Institute of Polymer Chemistry, College of Chemistry, Nankai University, Tianjin 300071, China*

Rui Wang – *The Centre of Nanoscale Science and Technology and Key Laboratory of Functional Polymer Materials, Institute of Polymer Chemistry, College of Chemistry, Nankai University, Tianjin 300071, China*

Yuping Gao – *The Centre of Nanoscale Science and Technology and Key Laboratory of Functional Polymer Materials, Institute of Polymer Chemistry, College of Chemistry, Nankai University, Tianjin 300071, China*

Yu Zou – *The Centre of Nanoscale Science and Technology and Key Laboratory of Functional Polymer Materials, Institute of Polymer Chemistry, College of Chemistry, Nankai University, Tianjin 300071, China*

Bin Kan – *School of Materials Science and Engineering, National Institute for Advanced Materials, Nankai University, Tianjin 300350, China*

Xiangjian Wan – *The Centre of Nanoscale Science and Technology and Key Laboratory of Functional Polymer Materials, Institute of Polymer Chemistry, College of Chemistry and Renewable Energy Conversion and Storage Center (RECAST), Nankai University, Tianjin 300071, China; orcid.org/0000-0001-5266-8510*

Complete contact information is available at: <https://pubs.acs.org/doi/10.1021/jacs.3c12605>

Author Contributions

*Y.X. and H.L. contributed equally to this work.

Notes

The authors declare no competing financial interest.

■ ACKNOWLEDGMENTS

The authors gratefully acknowledge the financial support from the National Key Research and Development Program of China (Nos. 2019YFA0705900, 2022YFB4200400), the National Natural Science Foundation of China (Grants Nos. 52273182, 21935007, 52025033), and 111 Project (B12015). We are thankful for the beam time provided by the 1W1A station (Beijing Synchrotron Radiation Facility) for GIWAXS characterization.

■ REFERENCES

- (1) Zhang, G.; Lin, F.; Qi, F.; Heumüller, T.; Distler, A.; Egelhaaf, H. J.; Li, N.; Chow, P. C. Y.; Brabec, C. J.; Jen, A. K. Y.; Yip, H. L. Renewed Prospects for Organic Photovoltaics. *Chem. Rev.* **2022**, *122* (18), 14180–14274.
- (2) Zhang, G.; Zhao, J.; Chow, P. C. Y.; Jiang, K.; Zhang, J.; Zhu, Z.; Zhang, J.; Huang, F.; Yan, H. Nonfullerene Acceptor Molecules for Bulk Heterojunction Organic Solar Cells. *Chem. Rev.* **2018**, *118* (7), 3447–3507.
- (3) Wan, X.; Li, C.; Zhang, M.; Chen, Y. Acceptor-Donor-Acceptor Type Molecules for High Performance Organic Photovoltaics-Chemistry and Mechanism. *Chem. Soc. Rev.* **2020**, *49* (9), 2828–2842.
- (4) Günther, M.; Kazerouni, N.; Blätte, D.; Perea, J. D.; Thompson, B. C.; Ameri, T. Models and Mechanisms of Ternary Organic Solar Cells. *Nat. Rev. Mater.* **2023**, *8* (7), 456–471.
- (5) Liu, Y.; Liu, B.; Ma, C.; Huang, F.; Feng, G.; Chen, H.; Hou, J.; Yan, L.; Wei, Q.; Luo, Q.; Bao, Q.; Ma, W.; Liu, W.; Li, W.; Wan, X.; Hu, X.; Han, Y.; Li, Y.; Zhou, Y.; Zou, Y.; Chen, Y.; Liu, Y.; Meng, L.;

- Li, Y.; Chen, Y.; Tang, Z.; Hu, Z.; Zhang, Z.; Bo, Z. Recent Progress in Organic Solar Cells (Part II Device Engineering). *Sci. China Chem.* **2022**, *65* (8), 1457–1497.
- (6) Liu, Y.; Li, B.; Ma, C.; Huang, F.; Feng, G.; Chen, H.; Hou, J.; Yan, L.; Wei, Q.; Luo, Q.; Bao, Q.; Ma, W.; Liu, W.; Li, W.; Wan, X.; Hu, X.; Han, Y.; Li, Y.; Zhou, Y.; Zou, Y.; Chen, Y.; Li, Y.; Chen, Y.; Tang, Z.; Hu, Z.; Zhang, Z.; Bo, Z. Recent Progress in Organic Solar Cells (Part I Material Science). *Sci. China Chem.* **2022**, *65* (2), 224–268.
- (7) Zhang, M.; Guo, X.; Ma, W.; Ade, H.; Hou, J. A Large-Bandgap Conjugated Polymer for Versatile Photovoltaic Applications with High Performance. *Adv. Mater.* **2015**, *27* (31), 4655–4660.
- (8) Lin, Y.; Wang, J.; Zhang, Z.; Bai, H.; Li, Y.; Zhu, D.; Zhan, X. An Electron Acceptor Challenging Fullerenes for Efficient Polymer Solar Cells. *Adv. Mater.* **2015**, *27* (7), 1170–1174.
- (9) Meng, L.; Zhang, Y.; Wan, X.; Li, C.; Zhang, X.; Wang, Y.; Ke, X.; Xiao, Z.; Ding, L.; Xia, R.; Yip, H. L.; Cao, Y.; Chen, Y. Organic and Solution-Processed Tandem Solar Cells with 17.3% Efficiency. *Science* **2018**, *361* (6407), 1094–1098.
- (10) Yuan, J.; Zhang, Y.; Zhou, L.; Zhang, G.; Yip, H. L.; Lau, T.; Lu, X.; Zhu, C.; Peng, H.; Johnson, P.; Leclerc, M.; Cao, Y.; Ulanski, J.; Li, Y.; Zou, Y. Single-Junction Organic Solar Cell with over 15% Efficiency Using Fused-Ring Acceptor with Electron-Deficient Core. *Joule* **2019**, *3* (4), 1140–1151.
- (11) Li, C.; Zhou, J.; Song, J.; Xu, J.; Zhang, H.; Zhang, X.; Guo, J.; Zhu, L.; Wei, D.; Han, G.; Min, J.; Zhang, Y.; Xie, Z.; Yi, Y.; Yan, H.; Gao, F.; Liu, F.; Sun, Y. Non-Fullerene Acceptors with Branched Side Chains and Improved Molecular Packing to Exceed 18% Efficiency in Organic Solar Cells. *Nat. Energy* **2021**, *6* (6), 605–613.
- (12) Zhu, L.; Zhang, M.; Xu, J.; Li, C.; Yan, J.; Zhou, G.; Zhong, W.; Hao, T.; Song, J.; Xue, X.; Zhou, Z.; Zeng, R.; Zhu, H.; Chen, C.; MacKenzie, R. C. I.; Zou, Y.; Nelson, J.; Zhang, Y.; Sun, Y.; Liu, F. Single-Junction organic solar cells with over 19% efficiency enabled by a refined double-fibril network morphology. *Nat. Mater.* **2022**, *21* (6), 656–663.
- (13) Pang, B.; Liao, C.; Xu, X.; Yu, L.; Li, R.; Peng, Q. Benzo[d]thiazole Based Wide Bandgap Donor Polymers Enable 19.54% Efficiency Organic Solar Cells Along with Desirable Batch-to-Batch Reproducibility and General Applicability. *Adv. Mater.* **2023**, *35* (21), 2300631.
- (14) Chen, T.; Li, S.; Li, Y.; Chen, Z.; Wu, H.; Lin, Y.; Gao, Y.; Wang, M.; Ding, G.; Min, J.; Ma, Z.; Zhu, H.; Zuo, L.; Chen, H. Compromising Charge Generation and Recombination of Organic Photovoltaics with Mixed Diluent Strategy for Certified 19.4% Efficiency. *Adv. Mater.* **2023**, *35* (21), 2300400.
- (15) Duan, T.; Feng, W.; Li, Y.; Li, Z.; Zhang, Z.; Liang, H.; Chen, H.; Zhong, C.; Jeong, S.; Yang, C.; Chen, S.; Lu, S.; Rakitin, O. A.; Li, C.; Wan, X.; Kan, B.; Chen, Y. Electronic Configuration Tuning of Centrally Extended Non-Fullerene Acceptors Enabling Organic Solar Cells with Efficiency Approaching 19%. *Angew. Chem., Int. Ed.* **2023**, *62* (42), 202308832.
- (16) Xu, X.; Xiao, J.; Zhang, G.; Wei, L.; Jiao, X.; Yip, H. L.; Cao, Y. Interface-Enhanced Organic Solar Cells with Extrapolated Lifetimes of over 20 Years. *Sci. Bull.* **2020**, *65* (3), 208–216.
- (17) Du, X.; Heumueller, T.; Gruber, W.; Classen, A.; Unruh, T.; Li, N.; Brabec, C. J. Efficient Polymer Solar Cells Based on Non-Fullerene Acceptors with Potential Device Lifetime Approaching 10 Years. *Joule* **2019**, *3* (1), 215–226.
- (18) Li, Y.; Huang, B.; Zhang, X.; Ding, J.; Zhang, Y.; Xiao, L.; Wang, B.; Cheng, Q.; Huang, G.; Zhang, H.; Yang, Y.; Qi, X.; Zheng, Q.; Zhang, Y.; Qiu, X.; Liang, M.; Zhou, H. Lifetime over 10000 h for Organic Solar Cells with Ir/IrO_x Electron-Transporting Layer. *Nat. Commun.* **2023**, *14* (1), 1241.
- (19) Li, Y.; Huang, X.; Ding, K.; Sheriff, H. K. M.; Ye, L.; Liu, H.; Li, C.; Ade, H.; Forrest, S. R. Non-Fullerene Acceptor Organic Photovoltaics with Intrinsic Operational Lifetimes over 30 Years. *Nat. Commun.* **2021**, *12* (1), 5419.
- (20) Han, Y.; Dong, H.; Pan, W.; Liu, B.; Chen, X.; Huang, R.; Li, Z.; Li, F.; Luo, Q.; Zhang, J.; Wei, Z.; Ma, C. An Efficiency of 16.46% and a T80 Lifetime of Over 4000 h for the PM6:Y6 Inverted Organic Solar Cells Enabled by Surface Acid Treatment of the Zinc Oxide Electron Transporting Layer. *ACS Appl. Mater. Interfaces* **2021**, *13* (15), 17869–17881.
- (21) Fan, P.; Zhang, D.; Wu, Y.; Yu, J.; Russell, T. P. Polymer-Modified ZnO Nanoparticles as Electron Transport Layer for Polymer-Based Solar Cells. *Adv. Funct. Mater.* **2020**, *30* (32), 2002932.
- (22) Beek, W. J. E.; Wienk, M. M.; Kemerink, M.; Yang, X.; Janssen, R. A. J. Hybrid Zinc Oxide Conjugated Polymer Bulk Heterojunction Solar Cells. *J. Phys. Chem. B* **2005**, *109* (19), 9505–9516.
- (23) Liu, H.; Liu, Z.; Wang, S.; Huang, J.; Ju, H.; Chen, Q.; Yu, J.; Chen, H.; Li, C. Boosting Organic-Metal Oxide Heterojunction via Conjugated Small Molecules for Efficient and Stable Nonfullerene Polymer Solar Cells. *Adv. Energy Mater.* **2019**, *9* (34), 1900887.
- (24) Xu, J.; Chen, Z.; Zapfen, J. A.; Lee, C. S.; Zhang, W. Surface Engineering of ZnO Nanostructures for Semiconductor-Sensitized Solar Cells. *Adv. Mater.* **2014**, *26* (31), 5337–5367.
- (25) Liu, J.; Chen, S.; Qian, D.; Gautam, B. R.; Yang, G.; Zhao, J.; Bergqvist, J.; Zhang, F.; Ma, W.; Ade, H.; Inganäs, O.; Gundogdu, K.; Gao, F.; Yan, H. Fast Charge Separation in a Non-Fullerene Organic Solar Cell with a Small Driving Force. *Nat. Energy* **2016**, *1*, No. 16089.
- (26) Wang, Y.; Zheng, Z.; Wang, J.; Liu, X.; Ren, J.; An, C.; Zhang, S.; Hou, J. New Method for Preparing ZnO Layer for Efficient and Stable Organic Solar Cells. *Adv. Mater.* **2023**, *35* (5), 2208305.
- (27) Liu, X.; Zheng, Z.; Wang, J.; Wang, Y.; Xu, B.; Zhang, S.; Hou, J. Fluidic Manipulating of Printable Zinc Oxide for Flexible Organic Solar Cells. *Adv. Mater.* **2022**, *34* (3), 2106453.
- (28) Sun, Y.; Seo, J. H.; Takacs, C. J.; Seifert, J.; Heeger, A. J. Inverted Polymer Solar Cells Integrated with a Low-Temperature-Annealed Sol-Gel-Derived ZnO Film as an Electron Transport Layer. *Adv. Mater.* **2011**, *23* (14), 1679–1683.
- (29) Lee, B. R.; Jung, E. D.; Nam, Y. S.; Jung, M.; Park, J. S.; Lee, S.; Choi, H.; Ko, S. J.; Shin, N. R.; Kim, Y. K.; Kim, S. O.; Kim, J. Y.; Shin, H. J.; Cho, S.; Song, M. H. Amine-Based Polar Solvent Treatment for Highly Efficient Inverted Polymer Solar Cells. *Adv. Mater.* **2014**, *26* (3), 494–500.
- (30) Lee, B. R.; Lee, S.; Park, J. H.; Jung, E. D.; Yu, J. C.; Nam, Y. S.; Heo, J.; Kim, J. Y.; Kim, B. S.; Song, M. H. Amine-Based Interfacial Molecules for Inverted Polymer-Based Optoelectronic Devices. *Adv. Mater.* **2015**, *27* (23), 3553–3559.
- (31) Chen, S.; Small, C. E.; Amb, C. M.; Subbiah, J.; Lai, T.-H.; Tsang, S.-W.; Manders, J. R.; Reynolds, J. R.; So, F. Inverted Polymer Solar Cells with Reduced Interface Recombination. *Adv. Energy Mater.* **2012**, *2* (11), 1333–1337.
- (32) Li, S.; Fu, Q.; Meng, L.; Wan, X.; Ding, L.; Lu, G.; Lu, G.; Yao, Z.; Li, C.; Chen, Y. Achieving over 18% Efficiency Organic Solar Cell Enabled by a ZnO-Based Hybrid Electron Transport Layer with an Operational Lifetime up to 5 Years. *Angew. Chem., Int. Ed.* **2022**, *61* (34), 202207397.
- (33) Drouilly, C.; Krafft, J. M.; Averseng, F.; Casale, S.; Bazer-Bachi, D.; Chizallet, C.; Lecocq, V.; Vezin, H.; Lauron-Pernot, H.; Costentin, G. ZnO Oxygen Vacancies Formation and Filling Followed by in Situ Photoluminescence and in Situ EPR. *J. Phys. Chem. C* **2012**, *116* (40), 21297–21307.
- (34) Papani, G. P.; Silvestri, B.; Vitiello, G.; De Stefano, L.; Rea, I.; Luciani, G.; Aronne, A.; Andreone, A. Morphological, Structural, and Charge Transfer Properties of F-Doped ZnO: A Spectroscopic Investigation. *J. Phys. Chem. C* **2017**, *121* (29), 16012–16020.
- (35) Wang, S.; Li, Y.; Yang, J.; Wang, T.; Yang, B.; Cao, Q.; Pu, X.; Etagar, L.; Han, J.; Zhao, J.; Li, X.; Hagfeldt, A. Critical Role of Removing Impurities in Nickel Oxide on High-Efficiency and Long-Term Stability of Inverted Perovskite Solar Cells. *Angew. Chem., Int. Ed.* **2022**, *61* (18), 202116534.
- (36) Small, C. E.; Chen, S.; Subbiah, J.; Amb, C. M.; Tsang, S.-W.; Lai, T.-H.; Reynolds, J. R.; So, F. High-Efficiency Inverted Dithienogermole-Thienopyrrolodione-Based Polymer Solar Cells. *Nat. Photonics* **2012**, *6* (2), 115–120.

(37) Zhang, Y.; Du, G.; Wang, X.; Li, W.; Yang, X.; Ma, Y.; Zhao, B.; Yang, H.; Liu, D.; Yang, S. X-Ray Photoelectron Spectroscopy Study of ZnO Films Grown by Metal-Organic Chemical Vapor Deposition. *J. Cryst. Growth*. **2003**, *252* (1–3), 180–183.

(38) Kehrer, M.; Duchoslav, J.; Hinterreiter, A.; Cobet, M.; Mehic, A.; Stehrer, T.; Stifter, D. XPS Investigation on the Reactivity of Surface Imine Groups with TFAA. *Plasma Process. Polym.* **2019**, *16* (4), 1800160.

(39) Lin, Y.; Zhang, Y.; Magomedov, A.; Gkogkosi, E.; Zhang, J.; Zheng, X.; El-Labban, A.; Barlow, S.; Getautis, V.; Wang, E.; Tsetseris, L.; Marder, S. R.; McCulloch, I.; Anthopoulos, T. D. 18.73% Efficient and Stable Inverted Organic Photovoltaics Featuring a Hybrid Hole-Extraction Layer. *Mater. Horiz.* **2023**, *10* (4), 1292–1300.

(40) Yao, J.; Ding, S.; Zhang, R.; Bai, Y.; Zhou, Q.; Meng, L.; Solano, E.; Steele, J. A.; Roeffaers, M. B. J.; Gao, F.; Zhang, Z.; Li, Y. Fluorinated Perylene-Diimides: Cathode Interlayers Facilitating Carrier Collection for High-Performance Organic Solar Cells. *Adv. Mater.* **2022**, *34* (32), 2203690.

(41) Ma, Y.; Zhang, M.; Wan, S.; Yin, P.; Wang, P.; Cai, D.; Liu, F.; Zheng, Q. Efficient Organic Solar Cells from Molecular Orientation Control of M-Series Acceptors. *Joule* **2021**, *5* (1), 197–209.

(42) Blom, P. W. M.; Mihailetschi, V. D.; Koster, L. J. A.; Markov, D. E. Device Physics of Polymer:Fullerene Bulk Heterojunction Solar Cells. *Adv. Mater.* **2007**, *19* (12), 1551–1566.

(43) Afroz, M. A.; Aranda, C. A.; Tailor, N. K.; Yukta; Yadav, P.; Tavakoli, M. M.; Saliba, M.; Satapathi, S. Impedance Spectroscopy for Metal Halide Perovskite Single Crystals: Recent Advances, Challenges, and Solutions. *ACS Energy Lett.* **2021**, *6* (9), 3275–3286.

(44) Proctor, C. M.; Kuik, M.; Nguyen, T. Q. Charge Carrier Recombination in Organic Solar Cells. *Prog. Polym. Sci.* **2013**, *38* (12), 1941–1960.

(45) Vandewal, K.; Benduhn, J.; Nikolis, V. C. How to determine optical gaps and voltage losses in organic photovoltaic materials. *Sustain. Energy Fuels* **2018**, *2* (3), 538–544.

(46) Wetzelaer, G. J. A. H.; Blom, P. W. M. Diffusion-Driven Currents in Organic-Semiconductor Diodes. *Npg Asia Mater.* **2014**, *6* (7), e110.

(47) Zhang, X.; Yao, N.; Wang, R.; Li, Y.; Zhang, D.; Wu, G.; Zhou, J.; Li, X.; Zhang, H.; Zhang, J.; Wei, Z.; Zhang, C.; Zhou, H.; Zhang, F.; Zhang, Y. On the Understanding of Energy Loss and Device Fill Factor Trade-offs in Non-Fullerene Organic Solar Cells with Varied Energy Levels. *Nano Energy* **2020**, *75*, No. 105032.

(48) Smilgies, D. M. Scherrer Grain-Size Analysis Adapted to Grazing-Incidence Scattering with Area Detectors. *J. Appl. Crystallogr.* **2009**, *42*, 1030–1034.

(49) Lin, Y.; Zhao, F.; Wu, Y.; Chen, K.; Xia, Y.; Li, G.; Prasad, S. K. K.; Zhu, J.; Huo, L.; Bin, H.; Zhang, Z.; Guo, X.; Zhang, M.; Sun, Y.; Gao, F.; Wei, Z.; Ma, W.; Wang, C.; Hodgkiss, J.; Bo, Z.; Inganäs, O.; Li, Y.; Zhan, X. Mapping Polymer Donors toward High-Efficiency Fullerene Free Organic Solar Cells. *Adv. Mater.* **2017**, *29* (3), 1604155.

(50) Zhang, B.; Yang, F.; Chen, S.; Chen, H.; Zeng, G.; Shen, Y.; Li, Y.; Li, Y. Fluid Mechanics Inspired Sequential Blade-Coating for High-Performance Large-Area Organic Solar Modules. *Adv. Funct. Mater.* **2022**, *32* (29), 2202011.

(51) Zhang, Y.; Wu, B.; He, Y.; Deng, W.; Li, J.; Li, J.; Qiao, N.; Xing, Y.; Yuan, X.; Li, N.; Brabec, C. J.; Wu, H.; Lu, G.; Duan, C.; Huang, F.; Cao, Y. Layer-By-Layer Processed Binary All-Polymer Solar Cells with Efficiency over 16% Enabled by Finely Optimized Morphology. *Nano Energy* **2022**, *93*, No. 106858.

(52) He, Q.; Sheng, W.; Zhang, M.; Xu, G.; Zhu, P.; Zhang, H.; Yao, Z.; Gao, F.; Liu, F.; Liao, X.; Chen, Y. Revealing Morphology Evolution in Highly Efficient Bulk Heterojunction and Pseudo-Planar Heterojunction Solar Cells by Additives Treatment. *Adv. Energy Mater.* **2021**, *11* (7), 2003390.

Recommended by ACS

“T-shaped” Carbazole Alkylammonium Cation Passivation in Perovskite Solar Cells

Zhuojie Shi, Yi Hou, *et al.*

JANUARY 10, 2024

ACS ENERGY LETTERS

READ 

Molecular Engineering of Azahomofullerene-based Electron Transporting Materials for Efficient and Stable Perovskite Solar Cells

Rohit D. Chavan, Daniel Prochowicz, *et al.*

SEPTEMBER 22, 2023

CHEMISTRY OF MATERIALS

READ 

Ammonium Salt Assisted Crystallization for High Performance Two-Dimensional Lead-Free Perovskite Photodetector

Tao Huang, Weili Yu, *et al.*

APRIL 10, 2023

ACS APPLIED ELECTRONIC MATERIALS

READ 

Enhancing Photoresponse and Photocurrent of Integrated Perovskite/Organic Solar Cells via Layer-by-Layer Processing

Xiang He, Weijie Song, *et al.*

DECEMBER 30, 2022

ACS APPLIED ENERGY MATERIALS

READ 

Get More Suggestions >